ELSEVIER Mathematical Biosciences 153 (1998) 125–150

Mathematical Biosciences
an international journal

Mathematical modelling of juxtacrine cell signalling

Markus R. Owen [a,c,*], Jonathan A. Sherratt [b,c]

[a] *Department of Mathematics, University of Utah, Salt Lake City, UT 84112, USA*
[b] *Department of Mathematics, Heriot-Watt University, Edinburgh EH14 4AS, UK*
[c] *Mathematics Institute, University of Warwick, Coventry CV4 7AL, UK*

Received 26 January 1998; received in revised form 17 July 1998

Abstract

Juxtacrine signalling is emerging as an important means of cellular communication, in which signalling molecules anchored in the cell membrane bind to and activate receptors on the surface of immediately neighbouring cells. We develop a mathematical model to describe this process, consisting of a coupled system of ordinary differential equations, with one identical set of equations for each cell. We use a generic representation of ligand–receptor binding, and assume that binding exerts a positive feedback on the secretion of new receptors and ligand. By linearising the model equations about a homogeneous equilibrium, we categorise the range and extent of signal patterns as a function of parameters. We show in particular that the signal decay rate depends crucially on the form of the feedback functions, and can be made arbitrarily small by appropriate choice of feedback, for any set of kinetic parameters. As a specific example, we consider the application of our model to juxtacrine signalling by TGFα in response to epidermal wounding. We demonstrate that all the predictions of our linear analysis are confirmed in numerical simulations of the non-linear system, and discuss the implications for the healing response.

Keywords: Juxtacrine; Signal range; TGFα; Wound healing; Epidermis

* Corresponding author. Address: University of Utah, Department of Mathematics, Salt Lake City, UT 84112, USA. Tel.: +1-801 585 1638; fax: +1-801 581 4148; e-mail: owen@math.utah.edu.

0025-5564/98/$00.00
PII: S0025-5564(98)10034-2

1. Introduction

Juxtacrine signalling is emerging as an important means of cellular communication. Traditionally, the activity of cell signalling molecules has been divided into autocrine, paracrine and endocrine, meaning respectively that the molecule acts only on the cell that secreted it, on a group of neighbouring cells (via extracellular diffusion), and on all cells within a tissue (e.g., hormones). However, within the close-packed cellular structure of an epithelium, a fourth method of communication is possible, in which signalling molecules anchored in the cell membrane bind to and activate receptors on the surface of immediately neighbouring cells. This was termed 'juxtacrine signalling' by Massagué [1], and subsequently a large number of examples have been identified.

Some juxtacrine ligand molecules are simply the precursors of soluble paracrine ligands. Good examples of this are epidermal growth factor (EGF) and the closely related transforming growth factor-α (TGFα), which are initially secreted in membrane-bound forms and subsequently cleaved to give the soluble form [1,2]. Both anchored and soluble forms of these growth factors are able to bind to epidermal growth factor receptors (EGF-R), so that both juxtacrine and paracrine modes of signalling are possible. In fact, in the case of TGFα, the cleavage of the membrane-bound precursor is typically slower than its turnover, so that the juxtacrine signalling mode dominates. A related example is provided by tumour necrosis factor, which also exists in a membrane-bound precursor to the soluble form; both of these forms are active, although in this case they bind to different cell surface receptors [3]. Other juxtacrine ligands exist only in membrane-bound forms: for example the *Drosophila* proteins Boss and Delta, which bind selectively to the receptors Sevenless and Notch [4]. More comprehensive lists of juxtacrine signalling molecules are given in Refs. [5,6].

Explicit mathematical modelling of juxtacrine communication was first considered by Collier et al. [7]. They considered the pattern-forming potential of the Notch–Delta system, and derived conditions for the formation of spatial patterns. These are patterns with the semi-wavelength of a single cell, and such structures are indeed observed in neural development [8]. In this paper we investigate the different question of the range over which juxtacrine signals may be transmitted, and the speed of this transmission. This has been studied recently by Monk [9], in a model for juxtacrine signalling by members of the transforming growth factor-β family, which are important regulators in development [10]. Monk [9] presents numerical simulations and analytical arguments which suggest that there is an upper bound on the number of cells over which a given level of cell activation may be attained. Here, we present an analytical study of the rate at which signals decay in a more general model for juxtacrine signalling, which suggests that, in general, arbitrarily small signal decay rates are possible. Moreover our analysis determines a parameter regime

in which patterns will form, through a different mechanism from that studied by Collier et al. [7].

In order to illustrate our analysis, we will present, throughout the paper, numerical simulations of the particular case of TGFα-mediated juxtacrine signalling following epidermal wounding, and we now give a brief biological overview of this system. In adult mammals, epidermal wounds heal by a combination of cell crawling at the wound edge, and enhanced proliferation further back – see Ref. [11] for review. Although this combined mechanism of healing was established many years ago [12], the underlying molecular details remain unclear. TGFα is implicated as an important element of the process in humans, since normal human keratinocytes produce TGFα both in vivo and in vitro [13], and TGFα upregulates both migration and proliferation of keratinocytes in culture [14]. Moreover, Schultz et al. [15] have shown that addition of exogenous TGFα accelerates epithelial wound healing. TGFα is synthesised as a 160 amino acid membrane-bound precursor, pro-TGFα, with a half-life of about 2 h [16]. The 50 amino acid soluble form of TGFα is generated by cleavage of pro-TGFα, a process which has a half-life of about 4 h [1,2]. Therefore the membrane-bound precursor is the dominant form of TGFα making it an ideal case for studying the range over which juxtacrine signals can be transmitted. In practice, many different growth factors act in concert in epidermal wound healing [17], and the distance from the wound edge over which the TGFα signal is active is a key indicator of its importance in the overall repair process.

The structure of this paper is as follows. In Section 2, we describe our model and discuss parameter estimation for the epidermal wound healing case study. In Section 3, we present an analytical determination of signalling range, and then (Section 4) we discuss the rate at which different signalling profiles will be achieved. In Section 5, we extend this analysis to consider the range of possible signalling profiles, and their dependence on parameters. The biological implications are discussed in Section 6.

2. Development of a mathematical model

Our mathematical model has a very simple form conceptually, consisting of ordinary differential equations which represent ligand–receptor binding, with one set of these equations for each cell. We use a representation of ligand–receptor binding that is as generic as possible, based on the scheme illustrated in Fig. 1. Thus we assume that a single ligand molecule binds reversibly to a receptor on the cell surface, giving an occupied receptor that is internalised within the cell. In practice, new ligand and new receptors will be produced at the cell surface, through a combination of recycling, release from intracellular stores, and de novo production within the cell. This complex

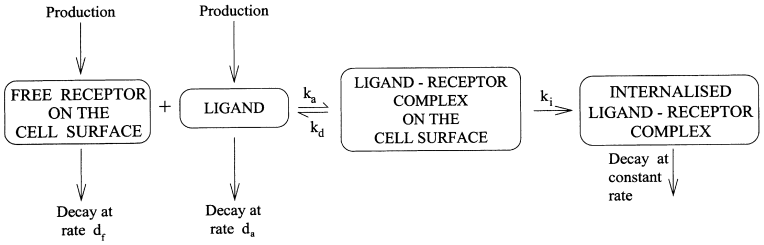

Fig. 1. A schematic representation of the kinetic scheme used in our model for the binding of ligand to receptors. The scheme is similar to that of Waters et al. [29] for EGF-EGF-R interactions. We base our parameters for the epidermal wound healing case study on the values they determined from experiments on the binding of EGF to EGF-R on rat lung epithelial cells.

series of processes has been modelled explicitly in a few specific cases [18,19], but we make the simplifying assumption that production of both ligand and receptor occurs at a rate that increases with the current level of occupied receptors. Such positive feedback is a central assumption in our model; it is well-documented for a number of ligand–receptor interactions, including the binding of N-formylated peptides to leucocytes [20], the binding of cAMP to *Dictyostelium* cells [19,21], and the binding of TGFα and EGF to EGF-R in keratinocytes [13,22,23].

We consider a two-dimensional epithelial sheet, which we represent as a regular array of identical, square cells. For simplicity, we restrict attention to the propagation of a signal away from a linear disturbance, so that the behaviour is one-dimensional, varying with cell number away from the disturbance; this is a natural first case to study in order to develop an understanding of juxtacrine signalling. For the example of epidermal wound healing, this case would represent well the propagation of elevated TGFα levels away from the edge of any reasonably large wound. Within a one-dimensional context, we anticipate that our assumption of a regular grid of square cells will be a fair approximation; however, experience from cellular automata models [24] indicates that the structure of two-dimensional behaviour would depend significantly on any imposed geometry of the cellular network.

Our model thus consists of a series of coupled ordinary differential equations for the numbers of ligand molecules $a_j(t)$, unoccupied receptors $f_j(t)$, and occupied receptors $b_j(t)$, on the surface of cells in row j, $j = 0, 1, 2, \ldots$; $j = 1$ corresponds to the cell row at the wound edge, and t denotes time. We assume that all of the ligand is anchored to the cell membrane. As discussed in Section 1, some growth factors that are primarily membrane bound can also be cleaved to give a freely diffusing form; however, we neglect this complication in order to focus on juxtacrine signalling in isolation. Using the kinetic scheme discussed above, the model equations are

$$\frac{\partial a_j}{\partial t} = -k_a a_j \frac{(f_{j-1} + 2f_j + f_{j+1})}{4} + k_d \frac{(b_{j-1} + 2b_j + b_{j+1})}{4} - d_a a_j + P_a(b_j), \quad \text{(1a)}$$

$$\frac{\partial f_j}{\partial t} = -k_a \frac{(a_{j-1} + 2a_j + a_{j+1})}{4} f_j + k_d b_j - d_f f_j + P_f(b_j), \quad \text{(1b)}$$

$$\frac{\partial b_j}{\partial t} = k_a \frac{(a_{j-1} + 2a_j + a_{j+1})}{4} f_j - k_d b_j - k_i b_j, \quad \text{(1c)}$$

($j \geqslant 1$). Here P_a and P_f represent the synthesis of TGFα and EGF-R, and will be discussed in detail below. Our assumption of juxtacrine communication is reflected by the use of averages of the concentrations of nearest neighbours in the ligand binding terms. These represent the overall number of ligand molecules and free and bound receptors on the surfaces of cells adjacent to those in row j. Within the context of our representation of the epithelium as a monolayer of square cells, two of the four cells adjacent to a cell in row j are also in row j, with the other two adjacent cells in rows $j-1$ and $j+1$. We neglect any variation in receptor or ligand densities over the surface of one cell, so that exactly $\frac{1}{4}$ of the receptors/ligand on each adjacent cell is available for binding to ligand/receptors on the original cell. In practice, receptors may move on the cell surface, while remaining bound within the cell membrane; this was modelled in Ref. [25]. This could lead to cell polarisation, and its inclusion is a natural extension of our model.

The synthesis of new ligand and receptor by epidermal cells is a crucial aspect of the model. As explained above, we assume that this is controlled by a positive feedback to the level of occupied receptors on the cell surface. Thus the production rates P_a of ligand and P_f of receptor are functions of the bound receptor number b_j. Our only assumption in general is that both of these production rates increase with b_j. In particular applications, the data available on production rates of ligand and receptors is typically extremely limited. However, the forms chosen for P_a and P_f can be specified to some extent because they must satisfy a number of conditions that relate them to quantities that are more easily measurable in experiments:

(i) In the absence of any ligand binding at the cell surface, there will be a background level of receptor expression, say r_0. This is a homogeneous steady state of the model, and so the equation for f in Eqs. (1a)–(1c) gives

$$P_f(0) = d_f r_0. \quad \text{(2a)}$$

(ii) Normal equilibrium levels of free and bound receptors, f_e and b_e say, are often known in particular systems. Specifying f_e and b_e defines the normal steady state level of free ligand, a_e, implicitly through Eq. (1c), as well as the values of the feedback functions at the steady state, so that

$$a_e = \frac{(k_d + k_i) b_e}{k_a f_e}, \quad P_a(b_e) = k_i b_e + d_a a_e, \quad P_f(b_e) = k_i b_e + d_f f_e. \quad \text{(2b)}$$

(iii) In any system, there will be a maximum possible level of receptor expression, r_m say. This can be estimated experimentally by saturating cells with ligand. Such saturation means that the rate of internalisation of bound receptors must be equal to the rate of free receptor production, giving

$$P_f(r_m) = k_i r_m. \tag{2c}$$

2.1. Case study: TGF-α signalling in epidermal wound healing

Our objective is to study the way in which a purely juxtacrine communication system transmits a signal away from a disturbance. Thus we are concerned with a semi-infinite array of cells, $0 \leqslant j < \infty$ say, with $a_j = a_e$, $f_j = f_e$, $b_j = b_e$ at $t = 0$ for $1 \leqslant j < \infty$, and with a boundary condition at $j = 0$ reflecting the imposed disturbance. We begin by describing the results of model simulations for our illustrative example, namely epidermal wound healing. Here $j = 1$ represents the wound edge, so that there are no cells in row 0; thus the appropriate boundary condition is

$$a_0 = f_0 = b_0 = 0. \tag{3}$$

We will not consider either movement or division of cells, so that there is no actual simulation of the healing process in the model; this has been the focus of previous mathematical models for epithelial wound healing [26–28]. We are simply concerned with the response of ligand (TGFα) and receptor (EGF-R) to the creation of the wound edge.

For the particular case of TGFα and EGF-R, there is extensive previous modelling work on which our parameter values can be based. In particular, we will use the results of Waters et al. [29] on epidermal growth factor (EGF) binding to EGF-R. This ligand–receptor interaction has in fact been modelled in considerable detail, including receptor cooperativity [30], intracellular ligand–receptor binding, and the details of internalisation via smooth and coated pits [31]. However, we neglect these details in the interests of simplicity, assumptions also made by Waters et al. [29].

Building on work by Wiley and co-workers in the 1980s [32–34], Waters et al. [29] performed in vitro experiments using foetal rat lung epithelial cells, to study the binding, dissociation, and internalisation of radiolabelled EGF; they used their data to estimate parameter values in an ordinary differential equation model. This model is the same as the kinetic component of Eqs. (1a)–(1c), except that, to simulate their experimental procedure, they assumed a constant rate of supply of free receptors and neglected cellular production of ligand. Their results determined the kinetic parameters as: binding, $k_a = 1.8 \times 10^8$ M^{-1} min^{-1}; dissociation, $k_d = 0.12$ min^{-1}; internalisation, $k_i = 0.19$ min^{-1}; and turnover of free receptors, $d_f = 0.03$ min^{-1}. EGF and TGFα are highly related growth factors, containing the same active domain

which binds to EGF-R, and thus we expect k_a, k_d and d_f to be roughly the same for the two proteins. However, we anticipate that the rate of internalisation k_i will be significantly lower for TGFα than for EGF since the latter is primarily in soluble form, while bound TGFα molecules will be attached via their transmembrane domain to a neighbouring cell; in the absence of any quantitative data, we take $k_i = 0.019\ \text{min}^{-1}$ for TGFα, a factor of 10 less than for EGF.

For the remaining parameters, we base the value of d_a on a detailed study of TGFα cleavage regulation [16], which suggests that the turnover time of TGFα is about 2 h, giving $d_a = 0.006\ \text{min}^{-1}$. We take the maximum possible number of EGF-R per cell, $r_m = 25\,000$, based on the experimental data of Oberg et al. [35], and assume that the unstimulated receptor number r_0, and equilibrium level of free and occupied receptors, f_e and b_e, are all 3000. These last three parameters are based on intuitive estimates, in the absence of quantitative experimental data. We leave parameters associated with the feedback functions P_a and P_f as free parameters, to be varied in model simulations.

We begin by describing simulations with Monod type feedback functions:

$$P_a(b) = \frac{C_1 b}{C_2 + b}, \qquad P_f(b) = C_3 + \frac{C_4 b}{C_5 + b}. \tag{4}$$

The qualitative difference between these functions reflects the intuitive expectation that in the complete absence of ligand binding, no ligand will be secreted, but that there will be a background level of receptor expression. The parameters $C_1,\ldots,C_5$ are constrained by conditions 2(a)–(c), leaving one free parameter, which we take as C_2, the number of bound receptors at which the ligand secretion rate attains half its maximum value. Numerical simulations of the model (1) with (4) and with the parameters described above show that the solution evolves to an equilibrium in which TGFα and occupied EGF-R levels increase away from the wound edge, with the free EGF-R level decreasing (Fig. 2). Moreover, the extent to which the perturbation at the wound edge is propagated away from that edge increases with the parameter C_2. This is consistent with intuitive expectation, since C_2 reflects the strength of positive feedback in TGFα production. In the remainder of the paper, we will study the model analytically, leading to a quantitative understanding of this relationship.

3. Predicting spatial decay rates

We wish to predict the rate at which large time solutions decay in space towards the homogeneous steady state – this homogeneous state is not a solution itself because of the wounded boundary condition at $j = 0$. Setting time derivatives to zero in Eqs. (1a)–(1c) gives three coupled difference equations:

$$0 = -k_a a_j \frac{(f_{j-1} + 2f_j + f_{j+1})}{4} + k_d \frac{(b_{j-1} + 2b_j + b_{j+1})}{4} - d_a a_j + P_a(b_j),$$

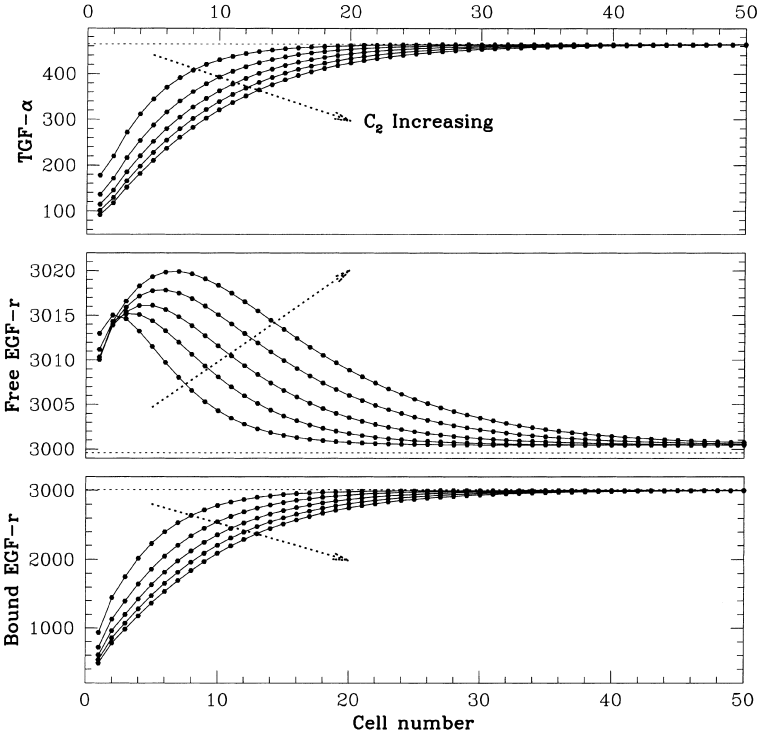

Fig. 2. Numerically calculated solutions of the model (1), specified with Eq. (4). The solutions are shown after 166.7 hours (10 000 minutes) of evolution with the wounded boundary condition (3), for C_2 increasing from 10 000 to 50 000 at intervals of 10 000. The distance of propagation of the wound-induced perturbation clearly increases as the parameter C_2, and hence the strength of feedback in TGFα production, increases. The other parameters are $k_a = 0.0003$ molecules^{-1} min^{-1}, $k_d = 0.12$ min^{-1}, $k_i = 0.019$ min^{-1}, $d_a = 0.006$ min^{-1}, $d_f = 0.03$ min^{-1}, $f_e = 3000$, $b_e = 3000$, $r_0 = 3000$, $r_m = 25500$. Although analytically we treat the domain as semi-infinite, we can only simulate a finite number of cells, N, and so we must specify an additional condition for cell $N+1$ – we use $u_{N+1} = u_N$. This is not significant provided N is sufficiently large; for this simulation, and those in subsequent figures, we use $N = 120$.

$$0 = -k_a \frac{(a_{j-1} + 2a_j + a_{j+1})}{4} f_j + k_d b_j - d_f f_j + P_f(b_j),$$

$$0 = k_a \frac{(a_{j-1} + 2a_j + a_{j+1})}{4} f_j - k_d b_j - k_i b_j.$$

Linearising about the homogeneous steady state (a_e, f_e, b_e) by setting $a_j = a_e + \tilde{a}_j$, $f_j = f_e + \tilde{f}_j$, $b_j = b_e + \tilde{b}_j$, gives

$$0 = -k_a f_e \tilde{a}_j - k_a a_e \frac{(\tilde{f}_{j-1} + 2\tilde{f}_j + \tilde{f}_{j+1})}{4} + k_d \frac{(\tilde{b}_{j-1} + 2\tilde{b}_j + \tilde{b}_{j+1})}{4} - d_a \tilde{a}_j + \mathscr{A}\tilde{b}_j,$$

$$0 = -k_a f_e \frac{(\tilde{a}_{j-1} + 2\tilde{a}_j + \tilde{a}_{j+1})}{4} - k_a a_e \tilde{f}_j + k_d \tilde{b}_j - d_f \tilde{f}_j + \mathscr{F} \tilde{b}_j,$$

$$0 = k_a f_e \frac{(\tilde{a}_{j-1} + 2\tilde{a}_j + \tilde{a}_{j+1})}{4} + k_a a_e \tilde{f}_j - k_d \tilde{b}_j - k_i \tilde{b}_j.$$

Here $\mathscr{A} = P_a'(b_e)$ and $\mathscr{F} = P_f'(b_e)$ are the slopes of the feedback functions at the normal steady state; we will show that these are key parameters in the control of signal range. We look for decaying solutions of the form $\tilde{a}_j = \bar{a} e^{\lambda L j}$, etc, where $\bar{a}$ is constant, and L is the length of an epidermal cell. Each of the bracketed terms for the contribution of neighbouring cells is then of the form

$$\frac{(\tilde{a}_{j-1} + 2\tilde{a}_j + \tilde{a}_{j+1})}{4} = \frac{\bar{a} e^{\lambda L(j-1)} + 2\bar{a} e^{\lambda L j} + \bar{a} e^{\lambda L(j+1)}}{4}$$
$$= \bar{a} e^{\lambda L j} \frac{(e^{-\lambda L} + 2 + e^{\lambda L})}{4},$$

with a corresponding reduction for b and f. For notational simplicity, we define

$$\mathscr{K}_d(\lambda) \equiv \frac{e^{\lambda L} + e^{-\lambda L} + 2}{4} = \frac{\cosh(\lambda L) + 1}{2}; \tag{5}$$

intuitively, this can be thought of as the 'nearest neighbour contribution' to the equilibrium. Substituting into the linearised equations, dividing throughout by $e^{\lambda L j}$, and collecting the terms in matrix form gives

$$\begin{pmatrix} -k_a f_e - d_a & -k_a a_e \mathscr{K}_d(\lambda) & k_d \mathscr{K}_d(\lambda) + \mathscr{A} \\ -k_a f_e \mathscr{K}_d(\lambda) & -k_a a_e - d_f & k_d + \mathscr{F} \\ k_a f_e \mathscr{K}_d(\lambda) & k_a a_e & -k_d - k_i \end{pmatrix} \begin{pmatrix} \bar{a} \\ \bar{f} \\ \bar{b} \end{pmatrix} = 0. \tag{6}$$

We wish to find non-trivial solutions, so we require the determinant of the matrix to be zero. Expanding the determinant gives a quadratic equation whose roots determine the values that $\mathscr{K}_d(\lambda)$ may take

$$\mathscr{K}_d(\lambda)^2 \{ d_f k_d + k_a k_i a_e - k_a a_e \mathscr{F} \} k_a f_e + \mathscr{K}_d(\lambda) \{ d_f k_a f_e \mathscr{A} \} - \{ d_f k_i + d_f k_d + k_a k_i a_e - \mathscr{F} \} (k_a f_e + d_a) = 0. \tag{7}$$

We denote the roots of Eq. (7) for $\mathscr{K}_d(\lambda)$ as $\mathscr{K}_+$ and $\mathscr{K}_-$. We can allow $\mathscr{K}_+$ and $\mathscr{K}_-$ to be complex, so that either both roots are real, or they are complex conjugates – the subscripts indicate that we order the roots with $\mathrm{Re}(\mathscr{K}_+) \geqslant \mathrm{Re}(\mathscr{K}_-)$. The set of permissible decay rates λ is given by the set of solutions of $\mathscr{K}_d(\lambda) = \{\mathscr{K}_+, \mathscr{K}_-\}$. Note that $\mathscr{K}_d$ is an even function of λ which is increasing with $|\lambda|$, so the decay rates will come in pairs of opposite sign, with the boundary condition selecting the direction of decay.

Turning now to the way the magnitude of the decay rate depends on parameters, we consider first the parameter C_2. It is straightforward to show that $\mathscr{A}$ increases with C_2, and thus the coefficient of $\mathscr{K}_d(\lambda)$ in Eq. (7) also increases.

The other coefficients are independent of C_2, and for the parameter set corresponding to TGFα–EGF-R, the coefficient of $\mathcal{K}_d(\lambda)^2$ is positive, and the constant term is negative, so that the positive solution $\mathcal{K}_+$ of Eq. (7) decreases. In turn this means that $|\lambda|$ decreases as C_2 increases, corresponding to a smaller rate of decay to the homogeneous steady state. This is consistent with the results illustrated in Fig. 2. Moreover, as C_2 tends to infinity, $\mathcal{A}$, and hence the coefficient of $\mathcal{K}_d(\lambda)$, tend to a finite limit. Again the other coefficients stay fixed, so that $\mathcal{K}_+$ will tend to a limit, and consequently the magnitude of the decay rate will be bounded below. Fig. 3 shows the variation of predicted decay rate

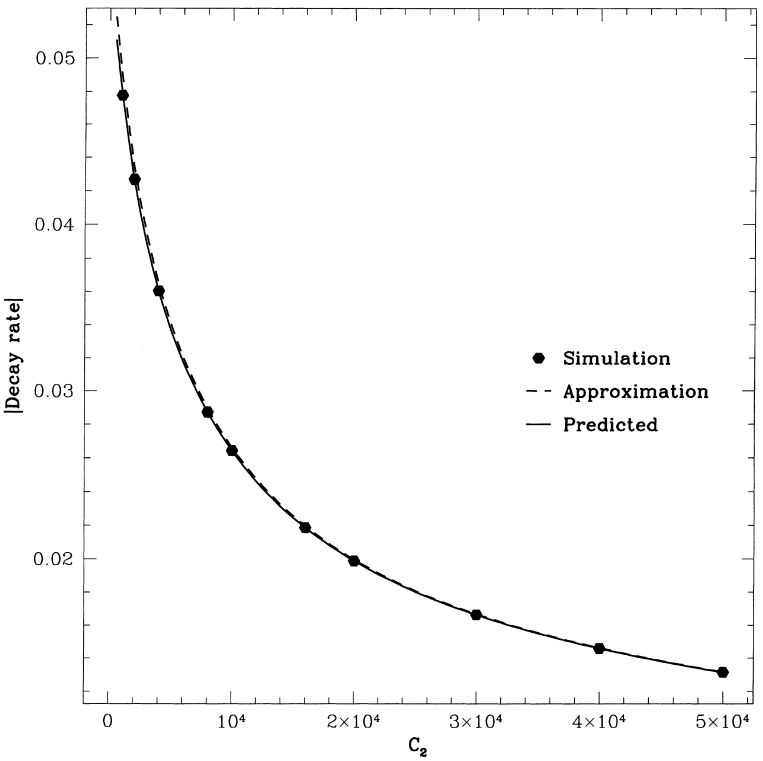

Fig. 3. Predicted magnitude of the decay rate as C_2 varies, for the steady state of the model (1), specified with Eq. (4) and the wounded boundary condition (3). The points represent decay rates calculated from simulation data 166.7 h (10 000 min) after wounding. The solid line indicates the decay rate predicted by linear analysis, which is given by the solution for λ of Eq. (7), where $\mathcal{K}_d(\lambda)$ is specified by Eq. (5). The dashed line shows the values given by a lowest order approximation to the decay rate Eq. (8), which is clearly very accurate. The other parameters are as in Fig. 2. The decay rate is estimated from the results of numerical simulations by using the formula (9) for each of the variables *a, f* and *b*, and calculating the point *j* where the norm of the differences between the rates is a minimum: specifically $\lambda_{\text{sim}} = (\lambda_a^j + \lambda_f^j + \lambda_b^j)/3$, where j is chosen such that $(\lambda_a^j - \lambda_f^j)^2 + (\lambda_a^j - \lambda_b^j)^2 + (\lambda_f^j - \lambda_b^j)^2$ is a minimum.

with C_2, together with decay rates calculated from numerical simulations of the model. Continuation of the curve of predicted decay rates, as C_2 increases further, confirms that the decay rate is bounded.

Another way to address these issues is to consider an approximation to the solution for the decay rates, so that we may get a more easily understandable relationship with parameters. In practice, we expect the decay rate to be small, $|\lambda| \ll 1$. Expanding $\mathscr{K}_d(\lambda)$ as a power series and substituting this into Eq. (7) gives to leading order

$$\lambda = \pm\frac{2}{L}\sqrt{\frac{d_a d_f(k_d+k_i)+k_a k_i(d_a a_e+d_f f_e)-d_f k_a f_e\mathscr{A}-d_a k_a a_e\mathscr{F}}{k_a f_e\left(2(d_f k_d+k_a k_i a_e)+d_f\mathscr{A}-2k_a a_e\mathscr{F}\right)}}. \tag{8}$$

We can see that increasing C_2, and hence $\mathscr{A}$, will decrease the numerator in the square root, and increase the denominator, so that the magnitude of the decay rate will decrease. Note that we have roots of either sign which correspond to the different directions of decay. One direction is selected by the boundary conditions which break the symmetry of the system – the wounded boundary condition (3) means that it is the negative root which is of interest. Fig. 3 includes this approximation to the predicted decay rate, and illustrates that it is highly accurate.

3.1. Calculating the decay rate from simulation data

In order to test the predictions we have made, we must generate numerical solutions to which we can make a comparison. Consider the proposed form for the solution, $a_j = a_e + \bar{a}e^{\lambda L j}, f_j = f_e + \bar{f}e^{\lambda L j}, b_j = b_e + \bar{b}e^{\lambda L j}$; then the decay rate calculated at the *jth* cell from the simulated solution for a_j, λ_a^j, is defined by

$$\lambda_a^j \equiv \frac{\ln\left|\frac{a_{j+1}-a_e}{a_j-a_e}\right|}{L} \approx \frac{\ln\left|\frac{\bar{a}e^{\lambda L(j+1)}}{\bar{a}e^{\lambda L j}}\right|}{L} = \frac{\ln(e^{\lambda L})}{L} = \lambda. \tag{9}$$

We expect the solution to have a transient near the wound edge, before approaching the normal steady state with the predicted decay rate, so that λ_a^j is expected to tend towards the predicted value as j tends to infinity. Of course, the calculated decay rate diverges as the steady state is approached, due to numerical errors. Hence there is a middle region, between the transients at the edge and the region of numerical inaccuracy, where we find useful information. The calculation is done in the above way for each variable – typical calculated decay rate profiles are shown in Fig. 4(a).

3.2. Generalized positive feedback may give zero signal decay

We have shown that for the feedback functions (4), the magnitude of the decay rate is bounded away from zero. However, the formula (8) implies that

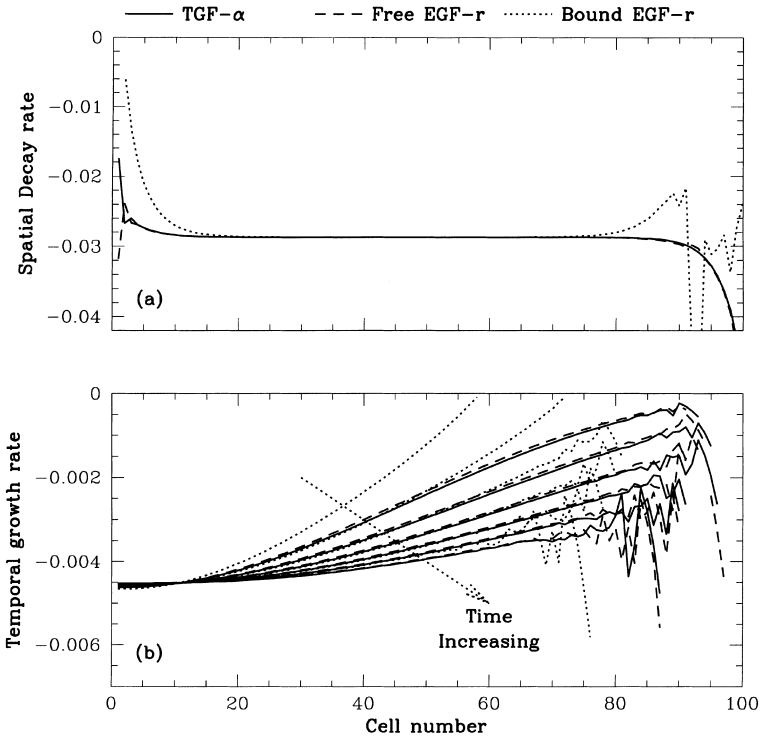

Fig. 4. (a) Typical profile of spatial decay rates for solutions of the juxtacrine model. The rates are calculated from simulation data using scheme (9), after 166.66̇ h (10 000 min), with $C_2 = 8000$. (b) Estimation of the temporal rate of growth to the spatially varying steady state. At each cell number the growth rate was calculated according to Eq. (15), using a previously generated solution from a simulation with the same parameters. The calculated growth rates are shown from 26.66̇ to 60 h at intervals of 6.66̇ h. As the solution evolves, the temporal growth rate seems to approach a constant level across the whole domain. The other model details and parameters are as in Fig. 2.

zero decay rates are possible for appropriate $\mathscr{A}$ and $\mathscr{F}$. To confirm this in simulations, we considered feedback functions of Hill form:

$$P_a(b) = \frac{C_1^m b^m}{C_2^m + b^m}, \quad \text{and} \quad P_f(b) = C_3 + \frac{C_4^n b^n}{C_5^n + b^n}. \tag{10}$$

As in the case $m = n = 1$ discussed in the previous section, the parameters C_1, C_3, C_4 and C_5 can be related to experimentally measurable quantities using Eqs. (2a)–(2c), leaving C_2, m and n as free parameters. In simulations of the model (1) with the parameter set corresponding to epidermal wound healing, we found that for m and n fixed at sufficiently large values (e.g. $m = n = 2$), increasing the parameter C_2 causes the magnitude of the decay rate to decrease,

apparently without bound, until at sufficiently large C_2, the normal steady state becomes unstable (not illustrated for brevity). In the following two sections, we will extend our linear analysis in order to explain this fundamental difference between $m = n = 1$ and large values of m and n, namely that decay rates are bounded in the former case and not in the latter.

4. Stability of the homogeneous equilibrium

Our objective in the remainder of the paper is to determine the form and rate of decay towards the homogeneous steady state that is implied by the model (1), as a function of parameter values. In view of the qualitative differences in behaviour described above for different Hill coefficients, we will treat the parameters $\mathscr{A}$ and $\mathscr{F}$ as dominant, and consider the behaviour in different regions of the $\mathscr{A}$–$\mathscr{F}$ plane. Recall that $\mathscr{A}$ and $\mathscr{F}$ are simply the slopes of the feedback functions at $b = b_e$. We begin, in this section, by investigating the temporal stability of the normal (homogeneous) steady state to homogeneous perturbations, since only stable equilibria will ever be seen in a biological context.

Linearising the model (1) as before about the spatially homogeneous steady state (a_e, f_e, b_e), but including time dependence, gives

$$\frac{\partial \tilde{a}}{\partial t} = -k_a f_e \tilde{a}_j - k_a a_e \frac{(\tilde{f}_{j-1} + 2\tilde{f}_j + \tilde{f}_{j+1})}{4} + k_d \frac{(\tilde{b}_{j-1} + 2\tilde{b}_j + \tilde{b}_{j+1})}{4} - d_a \tilde{a}_j + \mathscr{A}\tilde{b}_j,$$

$$\frac{\partial \tilde{f}}{\partial t} = -k_a f_e \frac{(\tilde{a}_{j-1} + 2\tilde{a}_j + \tilde{a}_{j+1})}{4} - k_a a_e \tilde{f}_j + k_d \tilde{b}_j - d_f \tilde{f}_j + \mathscr{F}\tilde{b}_j,$$

$$\frac{\partial \tilde{b}}{\partial t} = k_a f_e \frac{(\tilde{a}_{j-1} + 2\tilde{a}_j + \tilde{a}_{j+1})}{4} + k_a a_e \tilde{f}_j - k_d \tilde{b}_j - k_i \tilde{b}_j.$$

The condition for non-trivial solutions of the form $\big(\tilde{a}(t), \tilde{f}(t), \tilde{b}(t)\big) = (\bar{a}, \bar{f}, \bar{b})e^{\alpha t}$ can be easily derived as

$$\begin{aligned} Q(\alpha) \equiv\ & \alpha^3 + \alpha^2\big\{d_a + d_f + k_a a_e + k_a f_e + k_d + k_i\big\} \\ & + \alpha\big\{d_a d_f + (k_d + k_i)(d_a + d_f) + k_a a_e (d_a + k_i) \\ & + k_a f_e (d_f + k_i) - k_a f_e \mathscr{A} - k_a a_e \mathscr{F}\big\} + d_a d_f (k_d + k_i) \\ & + k_a k_i (d_a a_e + d_f f_e) - d_f k_a f_e \mathscr{A} - d_a k_a a_e \mathscr{F} \\ =\ & 0. \end{aligned}$$

The roots of this cubic characteristic equation determine the stability of the homogeneous steady state.

4.1. $\mathscr{L}_1$ and $\mathscr{L}_2$: Lines in $(\mathscr{A}, \mathscr{F})$ space which bound the region of temporal stability

The conditions for all the roots of a cubic polynomial of the form $\alpha^3 + a_1\alpha^2 + a_2\alpha + a_3$ to have negative real part are: $a_1 > 0$, $a_3 > 0$ and $a_1a_2 - a_3 > 0$. We clearly have $a_1 > 0$, and the remaining two conditions define curves in $(\mathscr{A}, \mathscr{F})$ space which delimit the relevant regions. Algebraic simplification shows that these curves are in fact straight lines, which are respectively

$$\mathscr{L}_1\colon\ \mathscr{F} = k_i + \frac{d_f(k_d + k_i)}{k_a a_e} + \frac{k_i d_f f_e}{d_a a_e} - \frac{d_f f_e}{d_a a_e}\mathscr{A}, \tag{11}$$

$$\mathscr{L}_2\colon\ \mathscr{F} = k_i + d_a + \frac{d_f f_e}{a_e} + \frac{d_a d_f + (k_d + k_i)(d_a + d_f)}{k_a a_e} + \frac{d_a^2(d_f + k_d + k_i) + (k_a a_e + k_a f_e + k_d + k_i + 1)k_a k_i f_e + (d_f f_e + d_a a_e)k_a}{(d_f + k_a a_e + k_a f_e + k_d + k_i)k_a a_e} - \frac{f_e(d_a + k_a a_e + k_a f_e + k_d + k_i)}{a_e(d_f + k_a a_e + k_a f_e + k_d + k_i)}\mathscr{A}. \tag{12}$$

These lines both have negative slope and are positive when $\mathscr{A} = 0$; the homogeneous steady state is stable if $\mathscr{A}$ and $\mathscr{F}$ lie on the same side of both lines as the origin. Fig. 5 illustrates that there are six possible geometries for this region, according to the relative slopes of the lines, and the location of their point of intersection. It is clear that the relative gradients of the two lines depend on the relationship between d_a and d_f. For $d_a < d_f$, independent of the other kinetic parameters, the line $\mathscr{L}_1$ has a more negative gradient than line $\mathscr{L}_2$; for $d_a > d_f$, the opposite is true. Moreover, the two lines intersect at

$$\mathscr{A} = k_i - \frac{d_a d_f}{d_f - d_a} - \frac{d_a^2 a_e}{(d_f - d_a)f_e} - \frac{d_a^2(d_f + k_d + k_i)}{(d_f - d_a)k_a f_e}, \tag{13a}$$

$$\mathscr{F} = k_i + \frac{d_f(d_a(d_f + k_a a_e) + d_f(k_a f_e + k_d + k_i))}{(d_f - d_a)k_a a_e}, \tag{13b}$$

so that for $d_a < d_f$ the intersection is for a positive value of $\mathscr{F}$, while for $d_a > d_f$ the intersection is for positive $\mathscr{A}$. These observations eliminate the cases (c) and (f) in Fig. 5 respectively, for any values of the kinetic parameters; this has important implications for the spatial decay rates, which will be described in the following section.

4.2. Predicting the temporal growth rate of a signal

The above calculation of the stability of an equilibrium state can also be used to estimate the rate at which a juxtacrine signal develops, following a localised disturbance such as wounding. This is a crucial issue, since a long signal range will not be significant if it takes a very long time to be established.

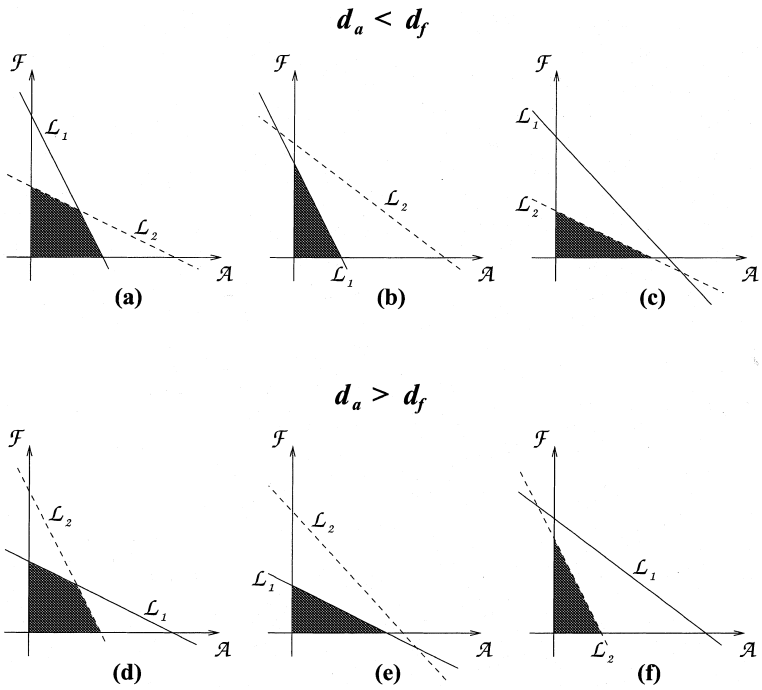

Fig. 5. A schematic illustration of the possible configurations of the lines $\mathscr{L}_1$ (solid) and $\mathscr{L}_2$ (dashed). The region under both lines is such that the normal steady state is temporally stable to homogeneous perturbations, and the solid line also coincides with a zero spatial decay rate. Parts (a),(b), and (c) are all the possibilities for $d_a < d_f$, since this implies that line $\mathscr{L}_1$ has a more negative slope than line $\mathscr{L}_2$. We can eliminate case (c) because we show in the main text that for $d_a < d_f$ the lines must intersect at a positive value of $\mathscr{F}$. Similarly for $d_a > d_f$ – cases (d), (e), and (f) – we can eliminate case (f) because the lines must intersect at a positive value of $\mathscr{A}$. We show in Section 5 that this means that whatever the kinetic parameters, it is never the case that an instability of the normal steady state can prevent solutions with zero decay rate.

We are concerned with the rate at which the solution decays to a spatially varying (decaying) state which, for sufficiently large j, will be very close to the homogeneous steady state. To leading order, this rate of decay is determined by the same eigenvalue equation $Q(\alpha) = 0$ as for the homogeneous steady state. For general perturbations, the rate will thus be determined by the root for α with least negative real part. For values of $\mathscr{A}$ and $\mathscr{F}$ close to the line $\mathscr{L}_1$, this root will be small in absolute value, and can thus be approximated by neglecting the α^2 and α^3 terms, giving

$$\begin{aligned}\alpha = &\left\{d_f k_a f_e \mathscr{A} + d_a k_a a_e \mathscr{F} - d_a d_f (k_d + k_i) - k_a k_i (d_a a_e + d_f f_e)\right\} \\ &\Big/ \left\{d_a d_f + (k_d + k_i)(d_a + d_f) + k_a a_e (d_a + k_i) \right. \\ &\left. + k_a f_e (d_f + k_i) - k_a f_e \mathscr{A} - k_a a_e \mathscr{F}\right\} . \end{aligned} \tag{14}$$

As expected, with the other parameters such that the homogeneous normal steady state is stable (corresponding to the shaded region in Fig. 5), this expression is negative, since the numerator is negative, and the denominator is positive. Note that the line $\mathscr{L}_1$ corresponds exactly to the numerator being equal to zero, and hence to a change in stability, as expected.

In order to compare these predictions with the results of numerical simulations, we determine the rate of convergence of a numerical solution to a numerically simulated steady state, determined as the long-time solution in a previous simulation for the same parameter set. Specifically, we define the temporal growth rate for the variable u at cell number j by

$$\alpha_{u,j} \equiv \frac{u_j(t+\delta_t) - u_j(t)}{\delta_t(u_j(t) - u_{j,\mathrm{ss}})}, \tag{15}$$

where $u_{j,\mathrm{ss}}$ denotes the numerically estimated long-term equilibrium. Fig. 4 includes an example of the somewhat subjective estimation given by this scheme for the rate of growth to the spatially varying steady state. We calculated $\alpha_{u,j}$ for each cell at every time step in our numerical simulations, and the figure shows the calculated values at constant intervals of time. As the solution evolves, the temporal growth rate seems to approach a level which is constant across the whole domain, but as the solutions approach the steady state within the limits of numerical accuracy, the calculated growth rates become wildly inaccurate. These results confirm the validity of Eq. (14), suggesting in fact that it is a good approximation for a wide range of parameter values, even for $\mathscr{A}$ and $\mathscr{F}$ fairly far from the line $\mathscr{L}_1$. Moreover, the results suggest that the approach to the spatially varying steady state occurs at approximately the same rate, whatever the location in space.

5. Analysis of spatially varying steady states

Having considered temporal stability, we now look in detail at the spatial decay rates λ in different parts of the $\mathscr{A}$–$\mathscr{F}$ plane, and the corresponding qualitative form of signal profile. Recall from Section 3 that the decay rates are determined as the roots for λ of $\mathscr{K}_d(\lambda) = \mathscr{K}_+$ and $\mathscr{K}_d = \mathscr{K}_-$, where $\mathscr{K}_\pm$ are the roots of the quadratic Eq. (7), with the 'nearest neighbour contribution' $\mathscr{K}_d$ defined in Eq. (5).

5.1. Zero spatial decay rates correspond to the line $\mathscr{L}_1$

We begin by considering the curve in $\mathscr{A}$–$\mathscr{F}$ space along which $\mathscr{K}_d(\lambda) = 1$, which corresponds to zero decay rates and hence unbounded signal range. Setting $\mathscr{K}_d(\lambda) = 1$ in Eq. (7) gives

$$\{d_f k_d + k_a k_i a_e - k_a a_e \mathscr{F}\} k_a f_e + \{d_f k_a f_e \mathscr{A}\}$$
$$- \{d_f k_i + d_f k_d + k_a k_i a_e - k_a a_e \mathscr{F}\}(k_a f_e + d_a) = 0$$

which when rearranged gives a line which is exactly the line $\mathscr{L}_1$ encountered above when analysing the temporal stability. This connection arises because solutions with zero decay rate are just uniform perturbations of the normal steady state, and so can only exist as steady states for the linearised system if the normal steady state has a zero eigenvalue, which corresponds exactly to the line $\mathscr{L}_1$. Thus the closer the parameters take us to this line, while remaining in the stable region already described, the smaller the decay rate will be. This result has a number of important implications. Firstly, recall that in Section 2 we described the observation of a lower bound on the magnitude of the decay rate when Hill-type feedback functions with $m = n = 1$ are used. The explanation for this is now straightforward: as the parameter C_2 increases, $\mathscr{A}$ approaches a limit which places the system at some finite distance from the line $\mathscr{L}_1$ in $(\mathscr{A}, \mathscr{F})$ space. Secondly, recall that in Section 4 we showed that of the various configurations of the lines $\mathscr{L}_1$ and $\mathscr{L}_2$ illustrated in Fig. 5, cases (c) and (f) do not arise for any parameter set. These are exactly the cases in which the domain of stability of the equilibrium state is bounded entirely by $\mathscr{L}_2$, and the fact that they cannot arise means that for any parameter set, arbitrarily small decay rates can be generated simply by altering the feedback functions in order to change $\mathscr{A}$ and $\mathscr{F}$.

5.2. $\mathscr{L}_3$ and $\mathscr{L}_4$: Lines in $(\mathscr{A}, \mathscr{F})$ space corresponding to zero coefficients in (7)

We have shown that the line $\mathscr{L}_1$ corresponds to one of $\mathscr{K}_\pm$ being 1. We now consider two other cases that give qualitative changes in behaviour, namely when one of $\mathscr{K}_\pm$ is infinite and when one is zero. The former case corresponds to the coefficient of $\mathscr{K}_d(\lambda)^2$ being zero in Eq. (7); this occurs on the line

$$\mathscr{L}_3: \quad \mathscr{F} = k_i + \frac{d_f k_d}{k_a a_e}. \tag{16}$$

The case of one of $\mathscr{K}_\pm$ being zero corresponds to the constant term in the quadratic Eq. (7) being zero, which occurs on the line

$$\mathscr{L}_4: \quad \mathscr{F} = k_i + \frac{d_f (k_d + k_i)}{k_a a_e} \tag{17}$$

which is clearly at a larger value of $\mathscr{F}$ than the line $\mathscr{L}_3$. For $\mathscr{F}$ above the value of $\mathscr{L}_4$, the constant term in the quadratic Eq. (7) will be positive.

5.3. $\mathscr{C}$: The curve in $(\mathscr{A}, \mathscr{F})$ space along which $\mathscr{K}_+ = \mathscr{K}_-$

Between the lines $\mathscr{L}_3$ and $\mathscr{L}_4$ lies a curve $\mathscr{C}$ which is the boundary of the region in which the roots $\mathscr{K}_\pm$ are complex. It is found by setting the discrim-

inant of the quadratic Eq. (7) to be zero – this curve $\mathscr{C}$ then corresponds to the locus of points where the quadratic has equal roots. It is given by

$$\mathscr{C}: \quad \mathscr{F} = k_i + \frac{d_f(2k_d + k_i)}{2k_a a_e} \pm \frac{d_f\sqrt{(d_a + k_a f_e)(k_i^2(d_a + k_a f_e) - k_a f_e \mathscr{A}^2)}}{2k_a a_e(d_a + k_a f_e)}, \tag{18}$$

note that when $\mathscr{A} = 0$, $\mathscr{C}$ coincides with the lines $\mathscr{L}_3$ and $\mathscr{L}_4$. In fact, the curve $\mathscr{C}$ is the envelope of the (straight line) contours of constant $\mathscr{K}_d(\lambda)$. Thus every line of equal $\mathscr{K}_d(\lambda)$ must lie tangent to it, and in particular the line $\mathscr{K}_d(\lambda) = 1$ (namely $\mathscr{L}_1$) touches it at the point

$$\mathscr{A} = \frac{2(d_a + k_a f_e)k_i}{d_a + 2k_a f_e}, \quad \mathscr{F} = k_i + \frac{d_f k_d}{k_a a_e} + \frac{k_i d_f(d_a + k_a f_e)}{k_a a_e(d_a + 2k_a f_e)}.$$

5.4. Fitting together these lines and curves in $(\mathscr{A}, \mathscr{F})$ space

We now consider the way in which $\mathscr{L}_3$, $\mathscr{L}_4$ and $\mathscr{C}$ fit into the possible arrangements of lines $\mathscr{L}_1$ and $\mathscr{L}_2$, namely cases (a), (b), (d) and (e) in Fig. 5. We consider this case by case below, and illustrate the results in Fig. 6.

Fig. 6(a): For $d_a < d_f$, straightforward examination shows that the line $\mathscr{L}_4$ is clearly at a smaller value of $\mathscr{F}$ than the point (13) at which lines $\mathscr{L}_1$ and $\mathscr{L}_2$ intersect. Hence line $\mathscr{L}_3$ must also lie below the intersection, and the curve of zero discriminant $\mathscr{C}$, because it intersects line $\mathscr{L}_1$ and lies between $\mathscr{L}_3$ and $\mathscr{L}_4$, must sit wholly within the stable region.

Fig. 6(b): Clearly from case (a) we know that the two lines and one curve lie at a smaller $\mathscr{F}$ value than at the intersection, but additionally it is clear that they lie at a smaller value of $\mathscr{F}$ than that at which line $\mathscr{L}_1$ intersects the axis, so that again the curve of zero discriminant $\mathscr{C}$, which touches the line $\mathscr{L}_1$, must sit wholly within the stable region.

Fig. 6(d): For $d_a > d_f$, straightforward examination shows that the lines $\mathscr{L}_3$ and $\mathscr{L}_4$ lie below the value of $\mathscr{F}$ at which line $\mathscr{L}_1$ intersects the axis, and above the value at which the lines $\mathscr{L}_1$ and $\mathscr{L}_2$ intersect. Again, the curve of zero discriminant $\mathscr{C}$, which touches the line $\mathscr{L}_1$, must sit wholly within the stable region.

Fig. 6(e): As for case (d), the lines and curves must lie below the value of $\mathscr{F}$ at which line $\mathscr{L}_1$ intersects the axis. However, in this case the intersection of lines $\mathscr{L}_1$ and $\mathscr{L}_2$ occurs for negative $\mathscr{F}$, and the lines and curves are all positive in the positive quadrant, so that again the curve of zero discriminant $\mathscr{C}$ must sit wholly within the stable region.

5.5. Steady state behaviour in the 5 regions specified

For each of these cases, the stable region is divided up by $\mathscr{L}_1, \ldots, \mathscr{L}_4$ and $\mathscr{C}$ into five regions, which are numbered in Fig. 6(a); the corresponding num-

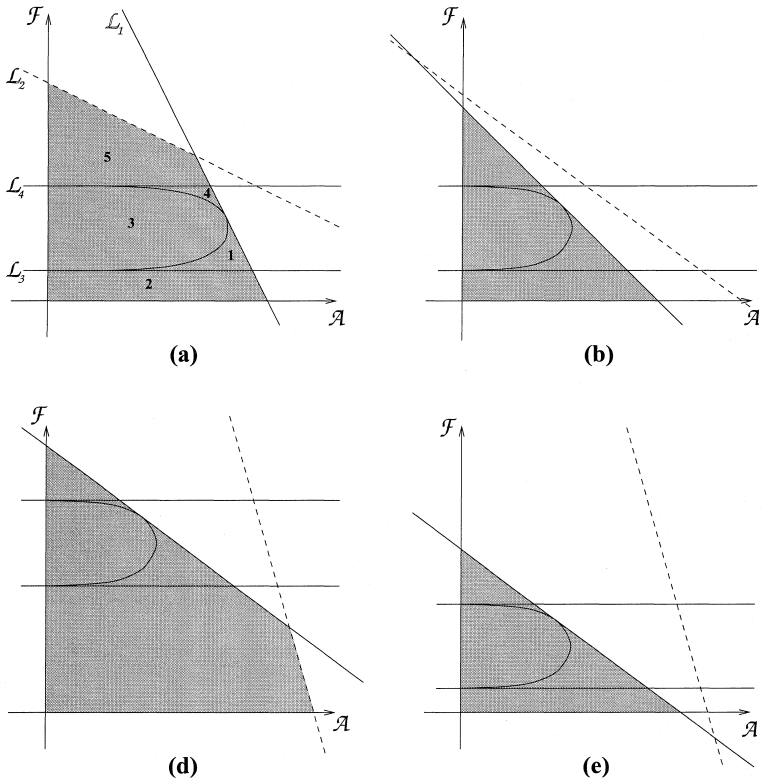

Fig. 6. Analytically derived lines $\mathscr{L}_1, \ldots, \mathscr{L}_4$, and the curve $\mathscr{C}$, delineating regions of different combinations of root types for $\mathscr{K}_+$ and $\mathscr{K}_-$. The numbers relate the regions to the cases analysed in the text. Cases (a), (b), (d) and (e) correspond to the four possible configurations of the two lines determining temporal stability to homogeneous perturbations.

bering scheme applies to the cases illustrated in parts (b), (d), and (e) of Fig. 6. We now consider the form of the roots of $\mathscr{K}_d(\lambda) = \mathscr{K}_\pm$ in each of these regions, and hence the qualitative form of the signalling profile. The solutions we give for λ can be derived from $\mathscr{K}_+$ and $\mathscr{K}_-$ by substituting $\lambda = \lambda_r + i\lambda_i$ into the expression (5) for $\mathscr{K}_d(\lambda)$, and equating real and imaginary parts. For notational simplicity, we give only roots for λ with negative real part; in all cases there are corresponding roots with positive real part.

Region 1: $\mathscr{K}_+, \mathscr{K}_- \in [1, \infty)$:

$$\Rightarrow \lambda \in \left\{ -\frac{\cosh^{-1}(2\mathscr{K}_+ - 1)}{L}, \; -\frac{\cosh^{-1}(2\mathscr{K}_- - 1)}{L} \right\}.$$

Each of these real eigenvalues corresponds to a monotonically decaying solution; the decay rate observed in practice will be the root with smallest absolute value. Examples of this monotonic signal decay are illustrated in Fig. 2.

Region 2: $\mathscr{K}_+ \in [1,\infty), \mathscr{K}_- \in (-\infty,0]$:

$$\Rightarrow \lambda \in \left\{ -\frac{\cosh^{-1}(2\mathscr{K}_+ - 1)}{L},\ -\frac{\cosh^{-1}(1-2\mathscr{K}_-) + i\pi}{L} \right\}.$$

The first of these solutions for λ corresponds to a monotonically decaying signal profile; the second represents a spatially oscillatory decay, with cells alternating between ligand/receptor levels above and below the homogeneous equilibrium. The solution observed in practice will be that corresponding to the root for λ whose real part has smallest absolute value, and it is straightforward to show that this must always be that corresponding to monotonic decay. To see this, note that taking cosh of both roots shows that the alternating root has the smallest real part if and only if $\mathscr{K}_+ + \mathscr{K}_- > 1$. Now the sum of the roots of the quadratic Eq. (7) is just $-\gamma/\beta$, where β and γ are the coefficients of $\mathscr{K}_d(\lambda)^2$ and $\mathscr{K}_d(\lambda)$ respectively, which are both positive in this region. Thus $\mathscr{K}_+ + \mathscr{K}_-$ is always negative, and so the alternating root cannot have the smallest real part.

Region 3: $\mathscr{K}_+, \mathscr{K}_-$ *complex*: $\mathscr{K}_+ = \mathscr{K}_r + i\mathscr{K}_i$ and $\mathscr{K}_- = \mathscr{K}_r - i\mathscr{K}_i$

$$\Rightarrow \lambda \in \{ -\lambda_{r,1} \pm (\lambda_{i,1})i,\ -\lambda_{r,2} \pm (\lambda_{i,2})i \},$$

where $\lambda_{r,1}$ and $\lambda_{r,2}$ are the solutions for λ_r of

$$\cosh^4(\lambda_r L) - 4(\mathscr{K}_i^2 - \mathscr{K}_r^2 + \mathscr{K}_r)\cosh^2(\lambda_r L) + (2\mathscr{K}_r - 1)^2 = 0,$$

and $\pm\lambda_{i,1}$ and $\pm\lambda_{i,2}$ are the solutions for λ_i of

$$\cos^4(\lambda_i L) - 2(2\mathscr{K}_i^2 + 2\mathscr{K}_r^2 - 2\mathscr{K}_r + 1)\cos^2(\lambda_i L) + (2\mathscr{K}_r - 1)^2 = 0.$$

In this case, the signal profiles exhibit an oscillatory decay in space, but with an oscillation wavelength that is not (in general) a whole number of cell lengths. This gives a complex decaying signal profile; an example is illustrated in Fig. 7.

Region 4: $\mathscr{K}_+, \mathscr{K}_- \in [0,1]$:

$$\Rightarrow \lambda \in \left\{ \frac{\cos^{-1}(2\mathscr{K}_+ - 1)}{L} i,\ \frac{\cos^{-1}(2\mathscr{K}_- - 1)}{L} i \right\}.$$

In this case, all the eigenvalues are purely imaginary, so that a decaying signal profile is not possible. Rather, all solutions are periodic in space, suggesting the possibility of patterned solutions. Of course, our analysis is only valid close to the homogeneous equilibrium, and thus does not guarantee that patterns will form in practice. However, spatial patterning is indeed the solution form we have observed in numerical simulations with $\mathscr{A}$ and $\mathscr{F}$ in this parameter region, as illustrated in Fig. 8. Intuitively, this pattern arises via a 'winner takes all' mechanism – neighbouring cells compete for ligand, and when more ligand binds to one particular cell, the effect is self-reinforcing because of the positive feedback in the system.

In common with all our numerical simulations, Fig. 8 was generated using parameters corresponding to epidermal wound healing; in this case, wounding induces a perturbation away from the normal steady state, which forms a

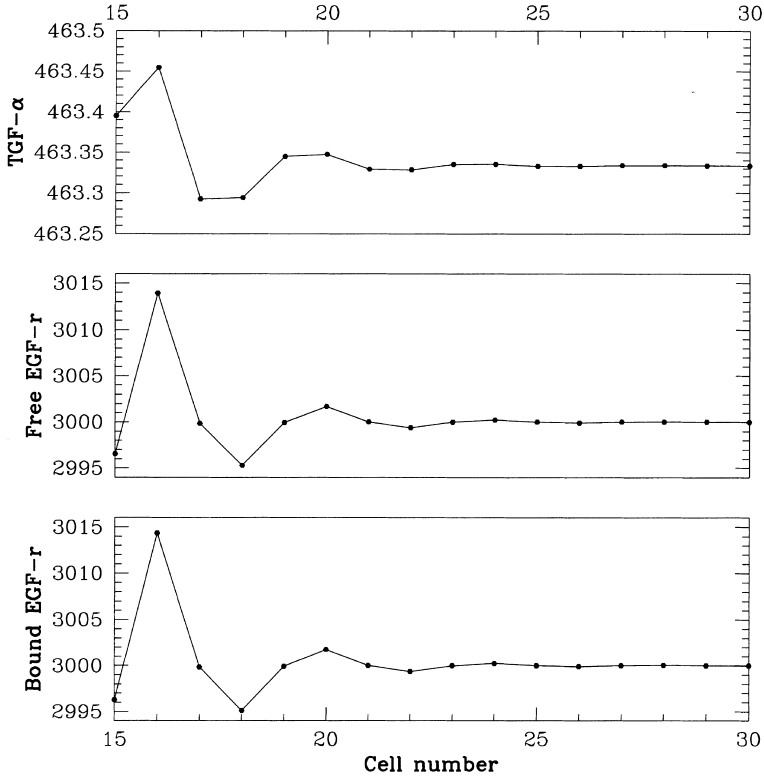

Fig. 7. Numerical simulation of the model (1), specified with Eqs. (2a)–(2c), and with Hill function feedbacks given by Eq. (10), with $m = 1.0$ and $n = 2.95$. Linear analysis predicts complex spatial eigenvalues, and hence oscillatory decay, corresponding to Region 3 of Fig. 6. The solid points and lines indicate the solution after 5000 h of evolution with the wounded boundary condition (3). The other parameters are $k_a = 0.0003$ molecules^{-1} min^{-1}, $k_d = 0.12$ min^{-1}, $k_i = 0.019$ min^{-1}, $d_a = 0.006$ min^{-1}, $d_f = 0.03$ min^{-1}, $f_e = 3000$, $b_e = 3000$, $r_0 = 3000$, $r_m = 25500$, $C_2 = 8000$..

growing pattern that reaches a stable, spatially patterned equilibrium. It is important to emphasise that the homogeneous equilibrium is also stable in this parameter regime. Nevertheless, when the wound boundary condition (3) is replaced by a symmetry boundary condition that is compatible with the homogeneous equilibrium, the pattern continues to grow (illustrated in Fig. 8), rather than receding, as a decaying signalling profile would.

Region 5: $\mathscr{K}_+ \in [0,1], \mathscr{K}_- \in (-\infty, 0]$:

$$\Rightarrow \lambda \in \left\{ \frac{\cos^{-1}(2\mathscr{K}_+ - 1)}{L} i,\ \pm \frac{\cosh^{-1}(1 - 2\mathscr{K}_-) + i\pi}{L} \right\}.$$

The first of these solutions corresponds to a spatially patterned solution, while the second corresponds to an oscillatory decay in signal, with oscillations

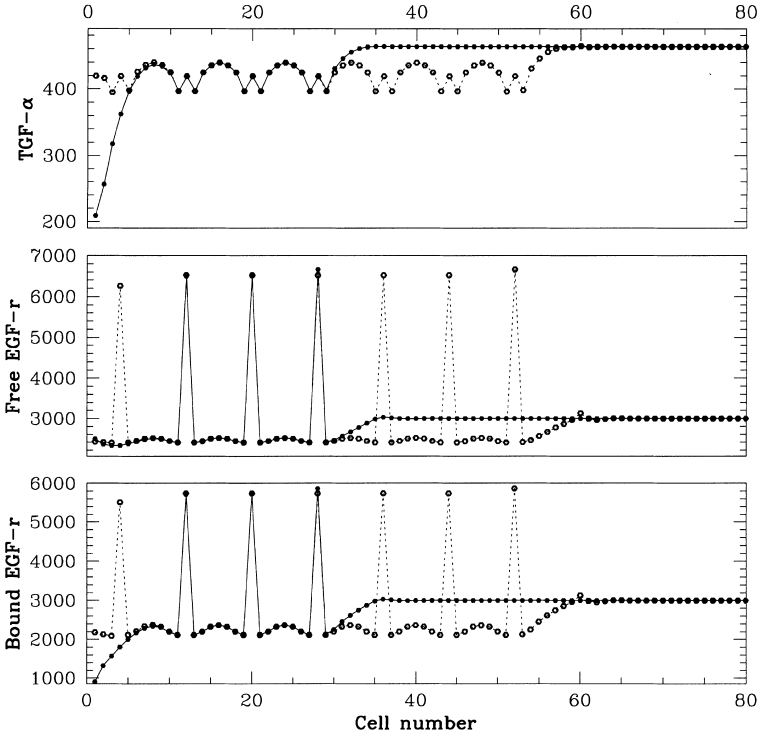

Fig. 8. Numerical simulation of the model (1), specified with Eqs. (2a)–(2c), and with Hill function feedbacks given by (10), with $m = 1.0$ and $n = 3.0$. Linear analysis predicts purely imaginary spatial eigenvalues, and hence pattern formation, corresponding to Region 4 of Fig. 6. The solid points and lines indicate the solution after 500 h of evolution with the wounded boundary condition (3). The open points and dotted lines indicate the solution a further 500 h after the introduction of a "healed" boundary condition $(a_0, f_0, b_0) = (a_1, f_1, b_1)$, which is compatible with the normal homogeneous steady state. Interestingly the patterned solution continues to persist and spread, in contrast to decaying solutions which recede to give the normal homogeneous steady state. The other parameters are $k_a = 0.0003$ molecules^{-1} min^{-1}, $k_d = 0.12$ min^{-1}, $k_i = 0.019$ min^{-1}, $d_a = 0.006$ min^{-1}, $d_f = 0.03$ min^{-1}, $f_e = 3000$, $b_e = 3000$, $r_0 = 3000$, $r_m = 25500$, $C_2 = 8000$..

having a period of two cell lengths. The purely imaginary eigenvalue has the real part of smallest magnitude (zero), so we expect this solution to dominate, giving patterned solutions similar to those seen in Region 4, and illustrated in Fig. 8.

Outside these five regions, the homogeneous steady state is unstable. We have concluded that solutions decay in Regions 1, 2 and 3, and that patterns form in Regions 4 and 5. Further analysis (not included here for brevity) shows that in its region of stability, the normal homogeneous steady state is always stable to inhomogeneous as well as homogeneous perturbations, except precisely in Regions 4 and 5.

6. Discussion

Juxtacrine signalling has the potential to generate signals which carry over a number of cell lengths, and the focus of this paper has been to quantify this phenomenon. We have shown that for any set of kinetic parameters, arbitrarily small signal decay rates can be generated by altering the feedback in ligand and receptor production, and we have characterised the qualitative form of signal profile predicted by the model, as a function of parameters.

Given the possibility of very long signal ranges, it is important to consider the time scales over which such solutions may develop. Our stability analysis shows that as the signal range increases, the rate at which solutions approach the steady state decreases, so that we may expect there to be some optimum pay-off between fast growth and long range. In this context, the key question is: for a given spatial location X, what is the parameter set giving maximal stimulation of a cell at that location at a given time T? The analysis in the main body of the text enables us to answer this question, at least within the context of the linear regime. The numerators of expressions (8) and (14), for the approximate spatial decay and temporal growth rates respectively, indicate that the temporal growth rate varies roughly in proportion to the square of the spatial decay rate. Thus the stimulation of a cell can be approximated by a perturbation of the form $Ae^{-\eta X}(1 - e^{a\eta^2 T})$, where we consider $\eta > 0$ to be the spatial decay rate – A and a are constants. For given X and T, this expression initially increases as η increases, reaching a maximum, after which it decreases. Thus we predict that there is trade-off between signal range and evolution time, with a compromise giving the maximal stimulation at a given point in space and time. However, numerical results from our wound healing simulations suggest that in practice, non-linear terms dominate the majority of the evolution once a wound is made, so that for realistic timescales, maximal stimulation is given by simply minimising the spatial decay rate η. Moreover, details of temporal evolution may be complicated by delays in the secretion of new receptor and ligand, arising from transcription and translation times, which may be significant on the time scale of juxtacrine signalling. Detailed modelling incorporating such delays is an important challenge for future work. However, the equilibrium behaviour, on which we have focussed in this paper, will not be affected by such delays.

We have seen that there is a regime in our model which gives spatial patterns propagating away from the wound edge. This is an important observation in view of the increasingly appreciated importance of juxtacrine signalling in developmental biology. Collier et al. [7] have previously studied a model for Delta–Notch signalling during development, which also exhibits spatial patterns. Their model is very different from ours because of the particular details of the Delta–Notch system; the model includes lateral inhibition of neighbouring cells via a feedback loop which is positive in one variable, and negative

in the other – in contrast to our model which has only positive feedback. This lateral inhibition was found to only give rise to patterning with a length scale of one or two cells, which is consistent with the fine-grained patterns seen in many developmental processes. However, patterns with a longer range have been characterised, for instance during neuroblast segregation in the Drosophila embryo [36], and Fig. 8 clearly illustrates that our model does admit the possibility of such solutions. A natural extension of this work would be to study the types of pattern seen in a fully two-dimensional model.

Throughout the paper, we have illustrated our results with numerical simulations using parameter values which correspond to juxtacrine signalling by TGFα (binding to EGF-R) in the epidermis, following wounding. This example is important because of the possibility that TGFα might play a significant role in coordinating the response of the epidermis to injury, which includes cell movement at the wound edge and significantly elevated proliferation in a band of cells around the wound (see Ref. [11] for review). In particular, it has been suggested that hair follicles are a possible source of regenerative keratinocyte stem cells [37]. Thus a key issue is whether TGFα signalling is sufficiently long-range to enable transmission of a signal between hair follicles (typical separation is 1–2 mm in humans). Our results enable this question to be answered if the form of the feedback functions were known, indicating that determination of these functions is an important goal for experiments.

Our modelling also suggests the use of in vitro experiments on cell sheets as a means of verifying predictions in any particular system. For example, in the wound healing context, 'wounding' of epithelial sheets derived from cultured keratinocytes is an established experimental procedure [38,39], which is closely related to our modelling framework. A detailed analysis of the protein kinetics in the remaining cells could be carried out, at least in principle, enabling direct comparison with model results. A key advantage of such a setup would be that the signalling kinetics would not be influenced by other cell types, wound healing mechanisms, and sources of protein. Within this framework, it would also be possible to manipulate rates of TGFα or EGF-R secretion, enabling verification of the predicted qualitative dependence of signal range on model parameters. The combination of such experiments and detailed mathematical modelling would enable a very detailed understanding of the juxtacrine signalling process.

Acknowledgements

M.R.O. was supported in part by an earmarked studentship from the Engineering and Physical Sciences Research Council. We thank Simon Myers and John Dallon for helpful discussions.

References

[1] J. Massagué, Transforming growth Factor-α: a model for membrane-anchored growth factors, J. Biol. Chem. 265 (1990) 21393.
[2] R. Brachmann, P.B. Lindquist, M. Nagashima, W. Kohr, T. Lipari, M. Napier, R. Derynck, Transmembrane TGF-α precursors activate EGF/TGF-α receptors, Cell 56 (1989) 691.
[3] M. Grell, E. Douni et al., The transmembrane form of tumour necrosis factor is the prime activating ligand of the 80 kDa tumour necrosis factor receptor, Cell 83 (1995).
[4] J. Lewis, Neurogenic genes and vertebrate neurogenesis, Curr. Op. Neurobiol. 6 (1996) 3.
[5] J. Massague, A. Pandiella, Membrane-anchored growth factors, Ann. Rev. Biochem. 62 (1993) 515.
[6] F. Fagotto, B.M. Gumbiner, Cell contact dependent signalling, Dev. Biol. 180 (1996) 445.
[7] J.R. Collier, N.A.M. Monk, P.K. Maini, J.H. Lewis, Pattern formation by lateral inhibition with feedback: A mathematical model of delta-notch intercellular signalling, J. Theor. Biol. 183 (1996) 429.
[8] S. Artavanis-Tsakonas, K. Matsuno, M.E. Fortini, Notch signalling, Science 268 (1995) 225.
[9] N.A.M. Monk, Restricted-range gradients and travelling fronts in a model of juxtacrine cell relay, submitted, 1998.
[10] N.A. Wall, B.L.M. Hogan, TGF-β related genes in development, Curr. Op. Genet. Dev. 4 (1994).
[11] J. Bereiter-Hahn, Epidermal cell migration and wound repair, in: J. Bereiter-Hahn, A.G. Matoltsy, K.S. Richards (Eds.), Biology of the Integument, Springer, New York, 1986, pp. 443.
[12] G.D. Winter, Epidermal regeneration studied in the domestic pig, in: H.I. Maibach, D.T. Rovee (Eds.), Epidermal Wound Healing, Year Book Med. Publ., Chicago, 1972, p. 71.
[13] R.J. Coffey, R. Derynck, J.N. Wilcox, T.S. Bringman, A.S. Goustin, H.L. Moses, M.R. Pittelkow, Production and auto-induction of transforming growth factor-α in human keratinocytes, Nature 328 (1987) 817.
[14] Y. Barrandon, H. Green, Cell migration is essential for sustained growth of keratinocyte colonies: The roles of transforming growth factor α and epidermal growth factor, Cell 50 (1987) 1131.
[15] G.S. Schultz, M. White, R. Mitchell, G. Brown, J. Lynch, D.R. Twardzik, G.J. Todardo, Epithelial wound healing enhanced by transforming growth factor-α and vaccinia growth factor, Science 235 (1987) 350.
[16] A. Pandiella, J. Massagué, Cleavage of the membrane precursor for transforming growth factor α is a regulated process, Proc. Natl. Acad. Sci. USA 88 (1991) 1726.
[17] P. Martin, J. Hopkinson-Woolley, J. McCluskey, Growth factors and cutaneous wound repair, Prog. Growth Factor Res. 4 (1992) 25.
[18] S.H. Zigmond, S.J. Sullivan, D.A. Lauffenburger, Kinetic analysis of chemotactic peptide receptor modulation, J. Cell. Biol. 92 (1982) 34.
[19] J.L. Martiel, A. Goldbeter, A model based on receptor desensitization for cyclic AMP signalling in Dictyostelium cells, Biophys. J. 52 (1987) 807.
[20] W. Zimmerli, B. Seligmann, J.I. Gallin, Exudation primes human and guinea pig neutrophils for subsequent responsiveness to chemotactic peptide N-FMLP and increases complement component C3bi receptor expression, J. Clin. Invest. 77 (1986) 925.
[21] J.C. Dallon, H.G. Othmer, A discrete cell model with adaptive signalling for aggregation of dictyostelium discoideum, Philos. Trans. R. Soc. Lond. B 352 (1997) 391.
[22] A.J.L. Clark, S. Ishii, N. Richert, G.T. Merlino, I. Pastan, Epidermal growth factor regulates the expression of its own receptor, Proc. Nat. Acad. Sci. USA 82 (1985) 8374.
[23] H.S. Earp, K.S. Austin, J. Blaisdell, R.A. Rubin, K.G. Nelson, L.W. Lee, J.W. Grisham, Epidermal growth factor (EGF) stimulates EGF receptor synthesis, J. Biol. Chem. 261 (1986) 4777.

[24] M. Markus, B. Hess, Isotropic cellular automaton for modeling excitable media, Nature 347 (1990) 56–58.
[25] M. Gex-Fabry, C. Delisi, Receptor mediated endocytosis: a model and its implications for experimental analysis, Am. J. Physiol. 247 (1984) R768–R779.
[26] J.A. Sherratt, J.D. Murray, Models of epidermal wound healing, Proc. R. Soc. Lond. B 241 (1990) 29.
[27] P.D. Dale, P.K. Maini, J.A. Sherratt, Mathematical modelling of corneal epithelial wound healing, Math. Biosci. 124 (1994) 127.
[28] D. Stekel, J. Rashbass, E.D. Williams, A computer graphic simulation of squamous epithelium, J. Theor. Biol. 175 (1995) 283.
[29] C.M. Waters, K.C. Oberg, G. Carpenter, K.A. Overholser, Rate constants for binding, dissociation, and internalization of EGF: effect of receptor occupancy and ligand concentration, Biochemistry 29 (1990) 3563.
[30] C. Wofsy, B. Goldstein, K. Lund, H.S. Wiley, Implications of epidermal growth factor (EGF) induced EGF receptor aggregation, Biophys J. 63 (1992) 98.
[31] C. Starbuck, D.A. Lauffenburger, Mathematical model for the effects of epidermal growth factor receptor trafficking dynamics on fibroblast proliferation response, Biotechnol. Prog. 8 (1992) 132.
[32] L.K. Opresko, H.S. Wiley, Receptor mediated endocytosis in xenopus oocytes i: characterization of the vitellogenin receptor system, J. Biol. Chem. 262 (1987) 4109.
[33] L.K. Opresko, H.S. Wiley, Receptor mediated endocytosis in xenopus oocytes ii: evidence for 2 novel mechanisms of hormonal regulation, J. Biol. Chem. 262 (1987) 4116.
[34] H.S. Wiley, D.D. Cunningham, A steady state model for analyzing the cellular binding, internalization and degradation of polypeptide ligands, Cell 25 (1981) 433.
[35] K.C. Oberg, A.M. Soderquist, G. Carpenter, Accumulation of epidermal growth factor receptors in retinoic acid treated fetal rat lung cells is due to enhanced receptor synthesis, Mol. Endocrinol. 10 (1988) 959.
[36] J.B. Skeath, S.B. Carroll, Regulation of proneural gene expression and cell fate during neuroblast segregation in the drosophila embryo, Development 114 (1992) 939.
[37] J.S. Yang, R.M. Lavker, T.T. Sun, Upper human hair follicle contains a subpopulation of keratinocytes with superior in vitro proliferative potential, J. Invest. Dermatol. 101 (1993) 652.
[38] I.M. Leigh, E.B. Lane, F.M. Watt (Eds.), The Keratinocyte Handbook, Cambridge University, Cambridge, 1994.
[39] J.M. Zahm, H. Kaplan, A.L. Herard, F. Doriot, D. Pierrotand, P. Somelette, E. Puchelle, Cell migration and proliferation during the in vitro wound repair of the respiratory epithelium, Cell. Motil. Cytoskel. (1997).